

The Thermal Sunyaev–Zel'dovich Effect from Massive, Quiescent $0.5 \le z \le 1.5$ Galaxies

Jeremy Meinke¹, Kathrin Böckmann², Seth Cohen³, Philip Mauskopf^{1,3}, Evan Scannapieco³, Richard Sarmento⁴, Emily Lunde³, and J'Neil Cottle³

Department of Physics, Arizona State University, P.O. Box 871504, Tempe, AZ 85287, USA

Universitat Hamburg, Hamburger Sternwarte, Gojebergsweg 112, D-21029, Hamburg, Germany

School of Earth and Space Exploration, Arizona State University, P.O. Box 876004, Tempe, AZ 85287, USA

United States Naval Academy, 121 Blake Road, Annapolis, MD, 21402, USA

Received 2020 November 3; revised 2021 February 26; accepted 2021 March 26; published 2021 May 27

Abstract

We use combined South Pole Telescope (SPT)+Planck temperature maps to analyze the circumgalactic medium (CGM) encompassing 138,235 massive, quiescent $0.5 \le z \le 1.5$ galaxies selected from data from the Dark Energy Survey (DES) and Wide-Field Infrared Survey Explorer (WISE). Images centered on these galaxies were cut from the 1.85 arcmin resolution maps with frequency bands at 95, 150, and 220 GHz. The images were stacked, filtered, and fit with a graybody dust model to isolate the thermal Sunyaev–Zel'dovich (tSZ) signal, which is proportional to the total energy contained in the CGM of the galaxies. We separated these $M_{\star}=10^{10.9}M_{\odot}-10^{12}M_{\odot}$ galaxies into 0.1 dex stellar mass bins, detecting tSZ per bin up to 5.6σ and a total signal-to-noise ratio of 10.1σ . We also detect dust with an overall signal-to-noise ratio of 9.8σ , which overwhelms the tSZ at 150 GHz more than in other lower-redshift studies. We corrected for the 0.16 dex uncertainty in the stellar mass measurements by parameter fitting for an unconvolved power-law energy-mass relation, $E_{\text{therm}}=E_{\text{therm,peak}}(M_{\star}/M_{\star,\text{peak}})^{\alpha}$, with the peak stellar mass distribution of our selected galaxies defined as $M_{\star,\text{peak}}=2.3\times10^{11}M_{\odot}$. This yields an $E_{\text{therm,peak}}=5.98^{+1.02}_{-1.00}\times10^{-60}$ erg and $\alpha=3.77^{+0.60}_{-0.74}$. These are consistent with $z\approx0$ observations and within the limits of moderate models of active galactic nucleus feedback. We also computed the radial profile of our full sample, which is similar to that recently measured at lower-redshift by Schaan et al.

Unified Astronomy Thesaurus concepts: Cosmic background radiation (317); Galaxy evolution (594); Intergalactic medium (813); Large-scale structure of the universe (902); Sunyaev-Zeldovich effect (1654); Quasars (1319)

1. Introduction

We have yet to understand the processes that shaped the history of the most massive galaxies in the universe. Each such galaxy is made up of a bulge of old, red stars surrounding a massive black hole, and the two are strongly connected. To be consistent with cosmological constraints, the lack of young stars in these galaxies requires active galactic nuclei (AGN) to have exerted significant feedback on their environment (Silk & Rees 1998; Granato et al. 2004; Scannapieco & Oh 2004; Croton et al. 2006; Bower et al. 2006). Without feedback from AGN, progressively more massive galaxies would form at later times (Rees & Ostriker 1977; White & Frenk 1991), in direct contrast with observations, which show that the typical mass of star-forming galaxies has been decreasing for the last ≈10 Gyr (Cowie et al. 1996; Treu et al. 2005; Drory & Alvarez 2008).

The details of AGN feedback remain uncertain, however. Two types of feedback models have been proposed. In "quasar-mode" feedback, the circumgalactic medium (CGM) is impacted by a powerful outburst that occurs when the supermassive black hole is accreting most rapidly. In this case, the CGM is heated to a high enough temperature and entropy that the gas-cooling time is much longer than the Hubble time, suppressing further star formation until today. Such models are supported by observations of high-velocity flows of ionized gas associated with the black holes accreting near the Eddington rate (Harrison et al. 2014; Greene et al. 2014; Lansbury et al. 2018; Miller et al. 2020), but the mass and energy flux from such a quasar is difficult to constrain due to uncertain estimates of the distance of the outflowing material from the central

source (Wampler et al. 1995; de Kool et al. 2001; Chartas et al. 2007; Feruglio et al. 2010; Dunn et al. 2010; Veilleux et al. 2013; Chamberlain et al. 2015).

In "radio-mode" feedback, on the other hand, cooling material is more gradually prevented from forming stars by jets of relativistic particles that arise during periods of lower accretion rates. In this case, the CGM is maintained at a roughly constant temperature and entropy, as low levels of gas cooling are continually balanced by energy input from the relativistic jets. Such models are supported by AGN observations of lower power jets of relativistic plasma (Fabian 2012). These couple efficiently to the volume-filling hot atmospheres of galaxies clusters (McNamara et al. 2000; Churazov et al. 2001; McNamara et al. 2016), but may or may not play a significant role in balancing cooling in less massive gravitational potentials (Werner et al. 2019).

One of the most promising methods for distinguishing between these models is by looking at anisotropies in the cosmic microwave background (CMB) photons passing through hot, ionized gas. If the gas is sufficiently heated, it will impose observable redshift-independent fluctuations in the CMB known as the thermal Sunyaev–Zel'dovich (tSZ) effect (Sunyaev & Zeldovich 1972). The resulting CMB anisotropy has a distinctive frequency dependence that causes a deficit of photons below $\nu_{\rm null}=217.6\,{\rm GHz}$ and an excess of photons above $\nu_{\rm null}$. The change in CMB temperature ΔT as a function of frequency due to the (nonrelativistic) tSZ effect is given by

$$\frac{\Delta T}{T_{\text{CMR}}} = y \left(x \frac{e^x + 1}{e^x - 1} - 4 \right),\tag{1}$$

where the dimensionless Compton-y parameter is defined as

$$y \equiv \int dl \ \sigma_T \frac{n_e k (T_e - T_{\text{CMB}})}{m_e c^2}, \tag{2}$$

where σ_T is the Thomson cross section, k is the Boltzmann constant, m_e is the electron mass, c is the speed of light, n_e is the electron number density, T_e is the electron temperature, $T_{\rm CMB}$ is the CMB temperature (we use $T_{\rm CMB} = 2.725$ K), the integral is performed over the line-of-sight distance l, and the dimensionless frequency x is given by $x \equiv h\nu/kT_{\rm CMB} = \nu/56.81$ GHz, where h is the Planck constant.

As the Compton-y parameter is proportional to both n_e and T, it provides a measure of the total pressure along the line of sight. By integrating the tSZ signal over a patch of sky, we can therefore obtain the volume integral of the pressure and calculate the total thermal energy $E_{\rm therm}$ in the CGM associated with a source (e.g., Scannapieco et al. 2008; Mroczkowski et al. 2019). As detailed in Spacek et al. (2016), this gives

$$E_{\text{therm}} = 2.9 \times 10^{60} \left(\frac{l_{\text{ang}}}{\text{Gpc}}\right)^2 \frac{\int \Delta y(\vec{\theta}) d\vec{\theta}}{10^{-6} \, \text{arcmin}^2},\tag{3}$$

where throughout this work, we adopt a Λ CDM cosmological model with parameters (from Planck Collaboration et al. 2020) $h=0.68,\,\Omega_0=0.31,\,\Omega_\Lambda=0.69,\,{\rm and}\,\,\Omega_b=0.049,\,{\rm where}\,\,h$ is the Hubble constant in units of 100 km s⁻¹ Mpc⁻¹, and $\Omega_0,\,\Omega_\Lambda,\,{\rm and}\,\,\Omega_b$ are the total matter, vacuum, and baryonic densities, respectively, in units of the critical density.

This relationship means that improvements in the sensitivity and angular resolution of tSZ measurements translate directly into improvements in constraints on thermal energy. Thus the cosmic structures with higher gas thermal energies, galaxy clusters, are most easily detected by tSZ measurements, and indeed, measurements of the tSZ effect over the last decade have been focused on detecting and characterizing these structures (e.g., Planck Collaboration et al. 2011; Reichardt et al. 2013; Planck Collaboration et al. 2016a; Hilton et al. 2018).

On the other hand, pushing to lower-mass halos has proven to be much more challenging. While in one case, evidence of a tSZ decrement caused by outflowing gas associated with a single luminous quasar was found in ALMA measurements (Lacy et al. 2019), most such constraints have involved averaging over many objects. In this regard, Chatterjee et al. (2010) used data from the Wilkinson Microwave Anisotropy Probe and Sloan Digital Sky Survey (SDSS) around both quasars and galaxies to find a tentative $\approx 2\sigma$ tSZ signal suggesting AGN feedback; Hand et al. (2011) used data from SDSS and the Atacama Cosmology Telescope (ACT) to find a $\approx 1\sigma - 3\sigma$ tSZ signal around galaxies; Gralla et al. (2014) used the ACT to find a $\approx 5\sigma$ tSZ signal around AGNs; Ruan et al. (2015) used SDSS and Planck to find $\approx 3.5\sigma - 5.0\sigma$ tSZ signals around both quasars and galaxies; Crichton et al. (2016) used SDSS and ACT to find a 3σ – 4σ SZ signal around quasars; Hojjati et al. (2017) used data from Planck and the Red Cluster Sequence Lensing Survey to find a $\approx 7\sigma$ tSZ signal suggestive of AGN feedback; and Hall et al. (2019) used ACT, Herschel, and Very Large Array data to measure the tSZ effect around ≈ 100 , 000 optically selected quasars, finding a 3.8σ signal that provided a joint constraint on AGN feedback and mass of the quasar host halos at $z \gtrsim 2$.

Recent measurements have also been made around massive galaxies. At $z \le 0.5$, Greco et al. (2015) used SDSS and Planck data to compute the average tSZ signal from a range of over 100,000 locally brightest galaxies (LBGs). This sample was large enough to derive constraints on E_{therm} as a function of galaxy stellar mass M_{\star} for objects with $M_{\star} \gtrsim 2 \times 10^{11} M_{\odot}$. More recently, Schaan et al. (2021) and Amodeo et al. (2021) combined microwave maps from ACT DR5 and Planck within the galaxy catalogs from the Baryon Oscillation Spectroscopic Survey (BOSS) to study the gas associated with these galaxy groups. They measured the tSZ signal at $\approx 10\sigma$ along with a weaker detection of the kinetic Sunyaev-Zel'dovich effect (Sunyaev & Zeldovich 1980), which constrains the gas density profile. They were able to compare these results to cosmological simulations (Battaglia et al. 2010; Springel et al. 2018) to find that the feedback employed in these models was insufficient to account for the gas heating observed at approximately megaparsec scales.

At redshifts $0.5 \lesssim z \lesssim 1.5$, the SZ signal from massive quiescent galaxies was studied by Spacek et al. (2016, 2017). These are precisely the objects for which AGN feedback is thought to quench star formation and thus where a significant excess tSZ signal is expected (e.g., Scannapieco et al. 2008). To obtain this faint signal, Spacek et al. (2016) performed a stacking analysis using VISTA Hemisphere Survey and Blanco Cosmology Survey data overlapping with 43 deg² at 150 and 220 GHz from the 2011 South Pole Telescope (SPT) data release, finding a $\approx 2-3\sigma$ signal that indicated nongravitational heating. Spacek et al. (2017) used SDSS and Wide-Field Infrared Survey Explorer (WISE) data overlapping with 312 deg² of 2008/2009 ACT data at 148 and 220 GHz, finding a marginal detection that was consistent with gravitational-only heating models.

Here we build on these measurements by making use of data from WISE, the Dark Energy Survey, and the 2500 square-degree survey of the southern sky taken by the SPT, which includes measurements at 95, 150, and 220 GHz. The increase in frequency and sky coverage allows us to obtain a 10.1σ detection of the tSZ effect around $z\approx 1$ galaxies. This lets us move from the marginal detections and upper limits presented in our previous work to measurements that can be applied to future simulations to strongly distinguish between feedback models.

The structure of this paper is as follows: In Section 2 we describe the data sets used for our analysis and compare them with our previous work. In Section 3 we describe our galaxy selection procedure, and the overall properties of the sample of massive, moderate-redshift, quiescent galaxies we use for the stacking analysis presented in Section 4. In Section 5 we compare our measurements with the work from other groups as well as with simple feedback models. Conclusions are given in Section 6.

2. Data

For our analysis, we use three public data sets, two to detect and select galaxies, and one to make our tSZ measurements. As discussed in Section 3, selecting and carrying out photometric fitting of passive galaxies at $0.5 \lesssim z \lesssim 1.5$ requires data that span optical, near-infrared, and mid-infrared wavelengths. Thus we make use of optical and near-infrared data from the DES data release 1 (Abbott et al. 2018), which are already matched to AllWISE data spanning 3–25 μ m (Schlafly et al. 2019). To

detect the tSZ effect, we use millimeter-wave observations from the SPT-SZ survey (Bocquet et al. 2019). The three data sets, which overlap over an area of \approx 2500 deg², are described in more detail below.

2.1. DES

The DES DR1 is based on optical and near-infrared imaging from 345 nights between 2013 August to 2016 February by the Dark Energy Camera mounted on the 4 m Blanco telescope at Cerro Tololo Inter-American Observatory in Chile. The data cover $\approx 5000~{\rm deg^2}$ of the southern Galactic cap in five photometric bands: grizY. These five bands have point-spread functions of g=1..12, r=0..96, i=0..88, z=0..84, and Y=0..90 full width at half maximum, FWHM (Abbott et al. 2018). The survey has exposure times of 90 s for griz and 45 s for Y band, yielding a typical single-epoch point-spread function (PSF) depth at a signal-to-noise ratio, S/N=10 for $g \lesssim 23.57$, $r \lesssim 23.34$, $i \lesssim 22.78$, $z \lesssim 22.10$, and $Y \lesssim 20.69$ mag (Abbott et al. 2018). Here and below, all magnitudes are quoted in the AB system (i.e., Oke & Gunn 1983).

2.2. WISE

The AllWISE catalog is based on the Wide-field Infrared Survey Explorer (WISE) NASA Earth orbit mission (Wright et al. 2010; Mainzer et al. 2011). In 2010 WISE carried out an all-sky survey of the sky in bands W1, W2, W3, and W4, centered at 3.4, 4.6, 12, and 22 μ m, respectively (Schlafly et al. 2019). The 40 cm diameter infrared telescope was equipped with four 1024×1024 pixel focal plane detector arrays cooled by a dual-stage solid-hydrogen cryostat. The whole sky was surveyed 1.2 times in all four bands at full sensitivity. After the hydrogen ice in the outer cryogen tank evaporated, WISE surveyed an additional third of the sky in three bands, with the W1 and W2 detectors operating at near full sensitivity, while the W3 focal plane operated at a lower sensitivity (Mainzer et al. 2011).

AllWISE uses the work of the WISE mission by combining data from the cryogenic and post-cryogenic survey, which yields a deeper coverage in W1 and W2. The added sensitivity of AllWISE extends the limit of detection of luminous distant galaxies because their apparent brightness at 4.6 μ m (W2) no longer declines significantly with increasing redshift. The increased sensitivity yields a better detection of these galaxies for redshift z > 1. This is crucial for our galaxy detection and selection because we are especially looking for luminous distant galaxies at a redshift z > 1.

2.3. SPT-SZ

The SPT-SZ survey (Chown et al. 2018) covers 2500 deg² of the southern sky between 2007 to 2011 in three different frequencies: 95 GHz and 150 GHz, which lie on either side of the maximum tSZ intensity decrement (\sim 128 GHz), and 220 GHz, which is very near $\nu_{\rm null} = 217.6$ GHz where there is no change in the CMB signal due to the tSZ effect. The South Pole Telescope (SPT) is a 10 m telescope located within 1 km of the geographical South Pole and consists of a 960-element bolometer array of superconducting transition-edge sensors. The maps used in this analysis are publicly available combined maps of the SPT with data from the all-sky Planck satellite (with similar bands at 100, 143, and 217 GHz). Each



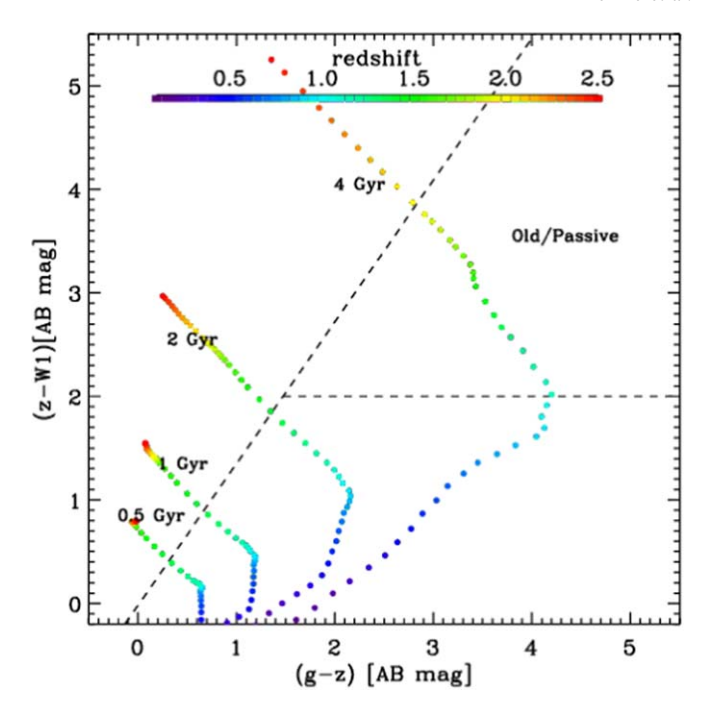


Figure 1. Color-color plot showing the selection region for passive galaxies. This is slightly modified from Spacek et al. (2017). These are BC03 models with age as indicated. This preselection is only used to query the DES database, with the final selection based on SED-fit parameters.

combined map has a beam resolution of 1.85 arcmin, and is provided in a HEALPix (Hierarchical Equal Area isoLatitude Pixelation) format with $N_{\rm side} = 8192$ (Chown et al. 2018). For comparison, the previous analysis of Spacek et al. (2016) relied on the 2011 SPT data release, covering a limited 95 deg² at only 150 and 220 GHz (Schaffer et al. 2011). The addition of the 95 GHz band allows for better extraction of the tSZ component, while the larger available field increases the galaxy sample size for reduced noise.

3. Defining the Galaxy Sample

3.1. Selection

We carried out our initial galaxy selection using the DES database server at NOAO, called NOAO-Lab. In order to start with a manageable sample, we applied a cut in color-color space designed to select old galaxies with low star formation rates at approximately $1.0 \le z \le 1.5$ in the initial database query, as shown in Figure 1. We used mag_auto from the DES in *grizy* bands, along with *W1* and *W2* PSF magnitudes (converted into the AB system) from AllWISE (Wright et al. 2010; Mainzer et al. 2011) joined to the main DES table. The bands and color selection used here are slightly different than Spacek et al. (2017) used in SDSS Stripe 82.

The NOAO Data laboratory allows direct queries in SQL via Jupyter notebook on their server. The lines we used to make the color selection were ($(mag_auto_z_dered-(w1mpro+2.699)) \le (1.37*mag_auto_g_dered-1.37*mag_auto_z_dered-0.02))$ and ($(mag_auto_z_dered-(w1mpro+2.699)) >= 2.0$).

3.2. Photometric Fitting

After the galaxies were selected, photometric redshifts were computed using EAZY (Brammer et al. 2008) and the seven

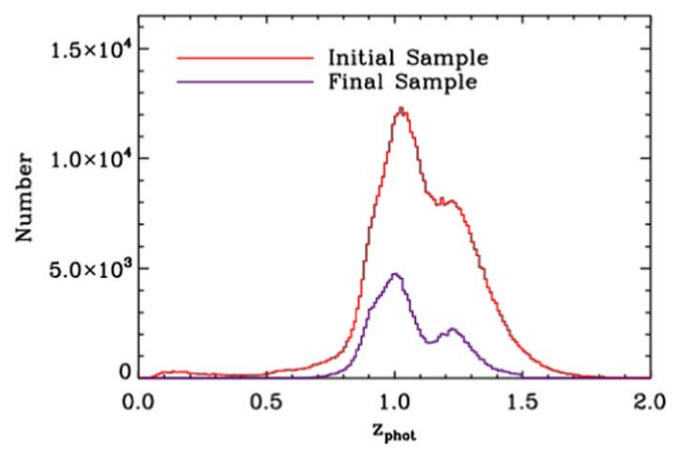


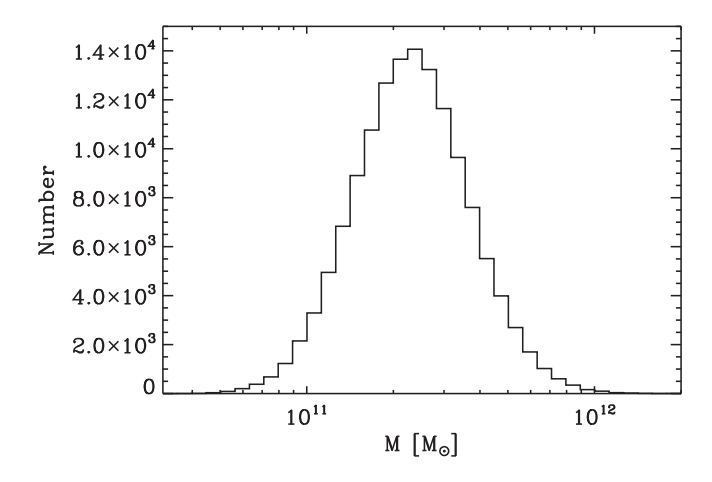
Figure 2. Six-band photometric redshift distribution of the initial color-selected sample (red). As expected, the majority of the sample is at z > 1. The final sample after selecting based on goodness of fit, redshift, age, and SSFR is shown in purple.

broad bands grizyW1W2. In calling EAZY, we used the CWW +KIN (Coleman et al. 1980; Kinney et al. 1996) templates, and did not allow for linear combinations. Because we are looking for red galaxies and have a gap in wavelength coverage between y band and W1, we were worried that allowing combinations of templates would yield unreliable redshifts, where, e.g., a red template was fit to the IR data and a blue one was fit to the optical data and they meet in the wavelength gap. The resulting redshift distribution is shown in Figure 2, which clearly shows that we selected galaxies in the desired range.

Once the redshifts were measured, we fit the spectral energy distributions (SEDs) using our own code, following the method used in Spacek et al. (2017), to which we refer for more details. Briefly, a grid of BC03 (Bruzual & Charlot 2003) models with exponentially declining star formation rates (SFRs) was fit over a range of stellar ages, star formation histories (SFHs; i.e., τ), and dust-extinction values (0 < A_V < 4). Our code uses BC03 models assuming a Salpeter initial mass function (IMF), but in comparison with the literature, we convert all stellar masses into the value assuming a Chabrier IMF (0.24 dex offset; Santini et al. (2015)). As in Spacek et al. (2017), we choose as our final sample all galaxies with age > 1 Gyr, SSFR < 0.01Gyr^{-1} , $0.5 < z_{\text{phot}} < 1.5$, and reduced $\chi^2 < 5$.

3.3. Removing Known Contaminants

Before using this catalog, several contaminants must be removed. We therefore remove sources from the ROSAT Bright and Faint Source catalogs (BSC and FSC; Voges et al. 1999). We additionally remove known clusters from ROSAT (Piffaretti et al. 2011) and Planck (Planck Collaboration et al. 2016b). Sources from the AKARI/FIS Bright Source Catalog (Yamamura et al. 2010) and the AKARI/IRC Point Source Catalog (Ishihara et al. 2010) were also removed along with galactic molecular clouds by cross-matching with the Planck Catalogue of Galactic Cold Clumps (Planck Collaboration et al. 2016c) and compact sources from the nine-band Planck Catalog of Compact Sources (Planck Collaboration et al. 2014). We also remove sources from the IRAS Point Source Catalog Joint Iras Science (1994). We do not remove the SZ sources selected from the SPT by Bleem et al. (2015). In all cases, sources with a possible contaminant within 4.0, to match the



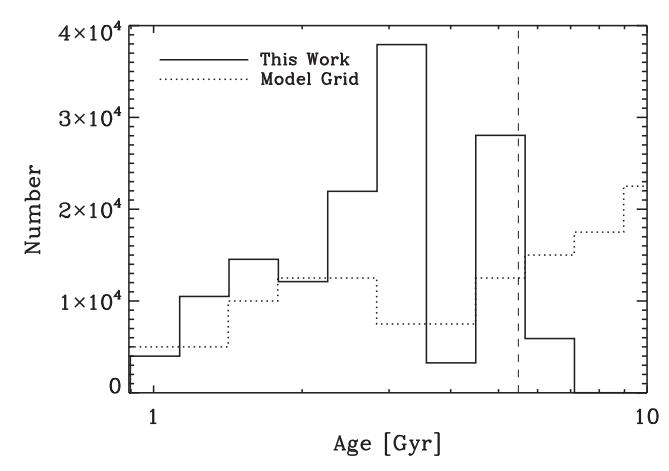


Figure 3. Top: Stellar mass distribution of the sample after selection based on SED parameters. Bottom: Age histogram of the sample. At a given redshift, the ages are restricted to be younger than the age of the universe at that redshift. The dashed black line shows the age of the universe at z = 1.1. The dotted line shows the scaled distribution of all available Bruzual & Charlot (2003) models on the grid.

beam of the SPT-SZ data, are flagged, and these sources are removed from further consideration. This left 138,235 massive and quiescent $z \gtrsim 0.5$ galaxies to include in our SZ stacks. This final sample is shown as the purple line in Figure 2, and the stellar mass distribution is shown in Figure 3. These galaxies were partitioned into 12 logarithmic stellar mass bins of width $\Delta \log_{10}(M_{\star}/M_{\odot}) = 0.1$ ranging from $\log_{10}(M_{\star}/M_{\odot}) = 10.9$ to 12.0. The mean and median redshift, mass, and angular-diameter-distance squared for each of these bins are listed in Table 1. These narrow-mass bins were chosen to more accurately fit the dust model discussed in Section 4, which has a dependence on redshift and potential nonlinearity with $\log_{10}(M_{\star}/M_{\odot})$.

3.4. Comparison with Previous Work

Our current sample has several advantages compared to our previous work in Spacek et al. (2016) and Spacek et al. (2017). As compared to Spacek et al. (2017), the DES data are deeper than the SDSS data, which provides for better SED fits in addition to fainter sources. In addition, the use of the AllWISE data is superior to the Wise All-Sky Survey (Wright et al. 2010) used in Spacek et al. (2017) because it includes more observing

Table 1 Statistics of 0.1 Wide Dex Stellar Mass Bins from $\log_{10}(M_*/M_{\odot}) = 10.9 - 12.0$

$\log_{10}(M_{\star}/M_{\odot})$ Bin	N	z	ĩ	$\log_{10}(\overline{M}/M_{\odot})$	$\log_{10}(\widetilde{M}/M_{\odot})$	Age [Gyr]	$\frac{\overline{l_{\rm ang}^2}}{[{\rm Gpc}^2]}$	$\widetilde{l}_{\text{ang}}^2$ [Gpc ²]
10.9 - 11.0	3376	0.94	0.95	10.96	10.96	1.69	2.76	2.78
11.0 - 11.1	8241	0.97	0.96	11.06	11.06	2.05	2.79	2.81
11.1 - 11.2	15738	1.00	0.98	11.16	11.16	2.47	2.83	2.84
11.2 - 11.3	23448	1.03	1.01	11.25	11.25	2.86	2.87	2.87
11.3 - 11.4	27723	1.07	1.04	11.35	11.35	3.19	2.91	2.91
11.4 - 11.5	24877	1.09	1.07	11.45	11.45	3.52	2.93	2.94
11.5 - 11.6	17246	1.11	1.09	11.55	11.54	3.71	2.95	2.96
11.6 - 11.7	9501	1.13	1.13	11.65	11.64	3.88	2.97	3.00
11.7 - 11.8	4396	1.15	1.16	11.74	11.74	4.01	2.99	3.03
11.8 - 11.9	1625	1.17	1.21	11.84	11.84	4.14	3.01	3.06
11.9 - 12.0	506	1.21	1.25	11.94	11.93	4.13	3.04	3.09

Note. Both mean and median are listed for redshift, mass, and angular-diameter-distance squared.

time from the extended NEOWISE mission (Mainzer et al. 2011). Again, this helps the fidelity of the SED fits. Second, we have slightly altered the color selection, as given above, so as to better include galaxies in the desired redshift range of $0.5 \leqslant z \leqslant 1.5$. This was successful, as shown in Figure 2, as compared to Figure 3 of Spacek et al. (2017).

The third difference is the choice of photometric redshift template. Our color selection aims to find very red galaxies because templates designed to work on the most general sets of galaxies are not ideal. This is mainly, but not only, due to large 4000 Å breaks. After testing all the available templates for EAZY, we found that the best fits were given by the empirical CWW+KIN templates because the elliptical galaxy template had a sufficiently large 4000 Å break. We found that 86% of our galaxies were best fit by either the E or Sbc CWW templates. By contrast, Spacek et al. (2017) used the EAZY V1.0 templates, which are based on population synthesis models.

Finally, Spacek et al. (2016) relied on the 2011 SPT data release covering a limited 95 \deg^2 at only 150 and 220 GHz (Schaffer et al. 2011), while the more recent data release used here both includes the 95 GHz band and covers a significantly larger area (2500 sq. deg.). This is also a much larger region than the \approx 300 \deg^2 of ACT data used in Spacek et al. (2017). All four of these improvements contribute to the far higher signal-to-noise ratio of the measurements in this work than our previous work.

4. Stacking and Filtering

To remove large-scale CMB and dust fluctuations, we applied a 5' high-pass Gaussian filter to each averaged

frequency stack. We used an iterative Gaussian method alongside the high-pass filter to minimize central signal loss in the process. This involved fitting the filtered stacked image center with a symmetric 2D Gaussian, subtracting this fit from the image prior to the high-pass filter, and repeating until no further central fit could be made. This cutoff was determined by the limit of either the Gaussian fit amplitude being lower than the surrounding image noise, or the Gaussian FWHM being fit with $<10\sigma$ certainty. The Gaussian FWHM fit was also constrained to a maximum of 1.5 times the map beam resolution (2.775 arcmin) to ensure no large or runaway fits, as a z = 1 galaxy would have an angular size ≈ 1 arcmin (for a diameter of 0.5 Mpc). The last iterative high-pass filter was then used on the original stacked image to produce the final averaged frequency images used for signal extraction.

To account for any residual bias offset from SPT maps, galaxy selection, and filtering procedure, we also generated a set of random points in the SPT field. After an identical 4-arcmin cut of contaminant sources, 869,878 random points were obtained. They were then stacked, averaged, and highpass filtered as outlined above for the galaxies. Measurements such as those listed in Section 5 include corrections obtained from these residual bias offsets. The stacked and filtered images around galaxies are illustrated in the upper panels of Figure 4, while the comparison stacks for the random points are illustrated in the lower panels of the figure. There is a clearly visible signal in the galaxy stacks that is not seen in the random stacks.

5. Results

5.1. Two-component Fitting

To extract the central signal from each filtered frequency stack, we used a circular top-hat aperture of 2'.0 radius. This is large enough to contain the majority of the central signal while minimizing noise introduced from any other surrounding sources. Additional apertures and sizes were also investigated, as detailed in Appendix B. To correct for beam and filter effects, we scaled all apertures with respect to $S_{\nu,\text{beam}}^{-1}$, where $S_{\nu,\text{beam}}$ is the aperture signal detected from a normalized central source convolved to the beam FWHM of 1'.85, and filtered as in Section 4. The final 2'.0 top-hat aperture used here has a

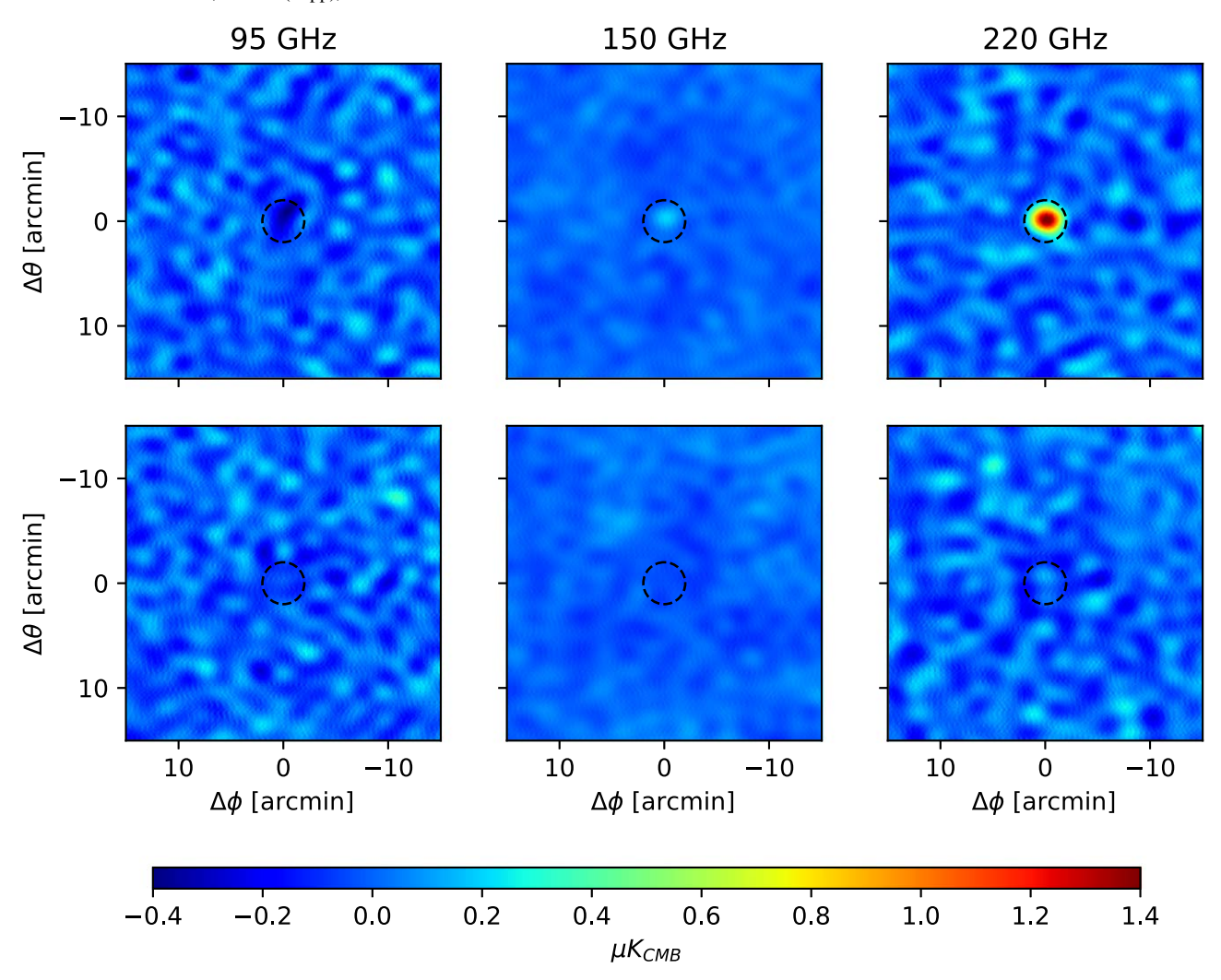


Figure 4. 30×30 arcmin filtered stacks at 95 (left), 150 (middle), and 220 (right) GHz for all (N = 138235) galaxies (top), and random points (bottom, N = 138235 out of the generated 869878). The center dashed circle in each represents the 2'.0 radius top-hat aperture discussed in Section 5.

Table 2
2'.0 Top-hat Integrated Temperatures Determined from Their Respective Frequency Stacks (95, 150, and 220 GHz) for 0.1 Wide dex Stellar Mass Bin Subsets of the Galaxy Catalog

$\log_{10}(M_{\star}/M_{\odot})$ Bin	$S_ u$	$= \int \Delta T_{\nu}(\vec{\theta}) d\vec{\theta} \ [\mu \text{K arcmin}^2]$]	$\int \! D_{220}(ec{ heta}) dec{ heta}$	$\int y(\vec{\theta})d\vec{\theta}$
810(*/)/ 2	95 GHz	150 GHz	220 GHz	$[\mu K \text{ arcmin}^2]$	[10 ⁻⁶ arcmin ²]
10.9–11.0	-3.66 ± 2.95	-0.02 ± 2.40	2.40 ± 3.80	$0.34^{+0.43}_{-0.44}$	$0.78^{+0.63}_{-0.63}$
11.0 - 11.1	-0.72 ± 1.89	2.20 ± 1.54	9.07 ± 2.44	$0.98^{+0.31}_{-0.33}$	$0.47^{+0.41}_{-0.42}$
11.1 - 11.2	-1.04 ± 1.37	2.15 ± 1.12	3.47 ± 1.77	$0.46^{+0.21}_{-0.22}$	$0.15^{+0.30}_{-0.30}$
11.2 - 11.3	-2.79 ± 1.13	-0.06 ± 0.92	5.73 ± 1.46	$0.57^{+0.18}_{-0.19}$	$0.87^{+0.25}_{-0.25}$
11.3-11.4	-1.55 ± 1.04	0.37 ± 0.85	5.37 ± 1.34	$0.50^{+0.15}_{-0.17}$	$0.59^{+0.23}_{-0.23}$
11.4–11.5	0.44 ± 1.10	3.72 ± 0.90	13.94 ± 1.42	$1.26^{+0.25}_{-0.30}$	$0.44^{+0.27}_{-0.28}$
11.5–11.6	-5.59 ± 1.31	-0.90 ± 1.07	9.28 ± 1.69	$0.80^{+0.21}_{-0.23}$	$1.69^{+0.29}_{-0.30}$
11.6 - 11.7	-4.16 ± 1.76	-0.07 ± 1.44	11.71 ± 2.27	$0.93^{+0.25}_{-0.29}$	$1.52^{+0.39}_{-0.40}$
11.7 - 11.8	-6.09 ± 2.58	-0.11 ± 2.10	17.59 ± 3.33	$1.34^{+0.37}_{-0.41}$	$2.27^{+0.57}_{-0.59}$
11.8 - 11.9	-2.66 ± 4.24	0.44 ± 3.46	26.14 ± 5.47	$1.75^{+0.53}_{-0.57}$	$2.23^{+0.94}_{-0.95}$
11.9 - 12.0	-15.52 ± 7.60	-7.53 ± 6.19	29.21 ± 9.79	$1.81^{+0.80}_{-0.84}$	$5.57^{+1.65}_{-1.65}$

Note. These values were extracted from the high-pass filtered stacks with the random point bias offsets subtracted, and scaled for beam correction. The last two columns show the dust and tSZ values obtained via component fit of Equation (4).

scale factor of 1.03, indicating that all but 3% of an unresolved central source is within the aperture. Table 2 lists the 2!0 tophat measurements after bias correction and scaling.

From our aperture measurements, we used a two-component fitting model consisting of tSZ (y) and z=0 dust in the 220 GHz band (D_{220}) ,

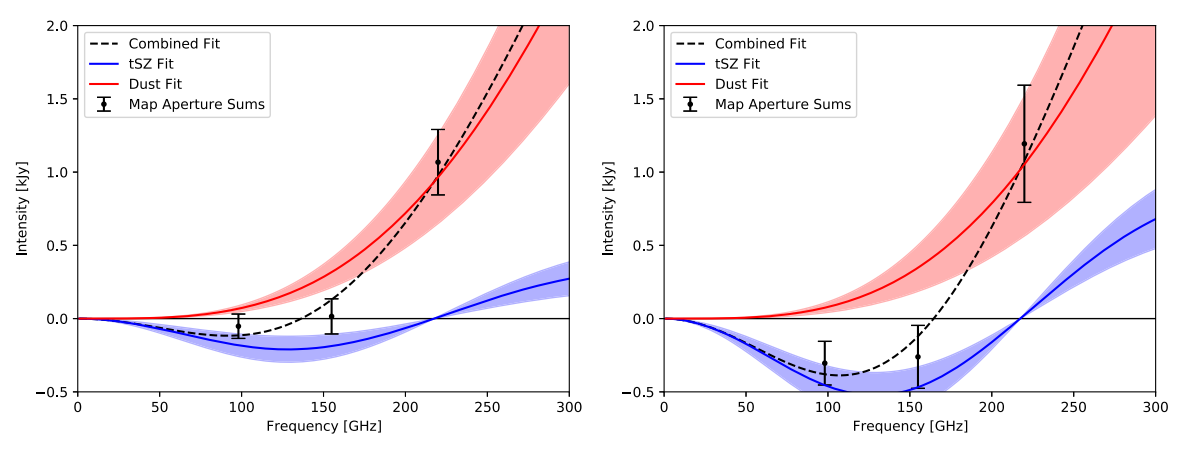


Figure 5. Intensity spectrum of our two-component fit for the two highest stellar mass bins $(\log_{10}(M_{\star}/M_{\odot}) = 11.8 - 11.9)$ and 11.9 - 12.0). The shaded tSZ and dust regions represent the 1σ error. The points are the 2/0 top-hat aperture values as listed in Table 2, placed at each frequency band center. Left: For $\log_{10}(M_{\star}/M_{\odot}) = 11.8 - 11.9$ bin (N = 1625 galaxies). Right: For $\log_{10}(M_{\star}/M_{\odot}) = 11.9 - 12.0$ bin (N = 506 galaxies).

$$S_{\nu} = \int \Delta T_{\nu}(\vec{\theta}) d\vec{\theta} = f_{x} \int y(\vec{\theta}) d\vec{\theta} + d_{\nu,220} \int D_{220}(\vec{\theta}) d\vec{\theta}, \quad (4)$$

where $f_x \equiv T_{\text{CMB}}[x(e^x+1)/(e^x-1)-4]$ of the tSZ signal (from Equation (1)), and $d_{\nu,220}$ is the graybody dust spectrum conversion from the CMB temperature at frequency band ν to the CMB temperature in the 220 GHz band at z=0,

$$d_{\nu,220} = \left[\frac{(1+z)\nu}{220\text{GHz}} \right]^{\beta} \frac{B[(1+z)\nu, T_{\text{dust}}]}{B(220\text{GHz}, T_{\text{dust}})} \frac{dT}{dB(\nu, T)} \bigg|_{T_{\text{CMB}}}$$

$$\frac{dB(220\text{GHz}, T)}{dT} \bigg|_{T_{CMB}}, \tag{5}$$

where β is the dust emissivity spectral index, and $B(\nu, T)$ is the Planck distribution. The tSZ and dust terms are integrated over SPT bandpasses extracted from Chown et al. (2018), as the SPT+Planck maps are dominated by the SPT response for our small angular scales (<5 arcmin). We use conservative values of $\beta = 1.75 \pm 0.25$ and $T_{\text{dust}} = 20 \pm 5$ K within the bounds of previous studies (Draine 2011; Addison et al. 2013; Planck Collaboration et al. 2014). Unlike investigations such as Greco et al. (2015), these values impact the final results due to our higher redshift and better map resolution, which lead to an increased dust detection at lower frequencies. We treat the dust parameters as Gaussian priors, fitting for a Gaussian distribution of β and T_{dust} with $\sigma_{\beta} = 0.25$ and $\sigma_{T_{\text{dust}}} = 5$. The reported best-fit y and D_{220} are the 50th percentile (median) obtained. Error from the priors are calculated as the bounds containing 1σ (68.27%), added in quadrature with the fit error. The uncertainty in our dust parameters determined in this way contributes up to 10% to our final reported errors.

The integrated aperture temperatures of Table 2 are fit according to Equation (4) with their median redshifts, yielding dust and tSZ signals as listed in the final two columns in this table. The dust is kept in units of μ K CMB at z=0 redshift and $\nu=220$ GHz for easy comparison, as dust is highest in the 220 GHz band.

We find a $0.8-4.2\sigma$ dust signal ranging between $0.34-1.81\mu\mathrm{K}$ arcmin² at 220 GHz for our mass bins. The highest dust S/N values occur in the higher-mass bins and show a trend of increasing dust with mass. The overall S/N detection of dust in our data is 9.8σ , and the dust fit is heavily

determined by the integrated 220 GHz values, which is also the noisiest of the three SPT bands.

For the tSZ signal, we see a negligible $0.5-3.5\sigma$ detection in the lower-mass bins between $10.9 \lesssim \log_{10}(M_\star/M_\odot) \lesssim 11.5$. From $\log_{10}(M_\star/M_\odot) = 11.5 - 12.0$, however, we observe an S/N up to 5.6σ . The four highest bins centered at 11.65, 11.75, 11.85, and 11.95 yield integrated y values of $1.52^{+0.39}_{-0.40}$, $2.27^{+0.57}_{-0.59}$, $2.23^{+0.94}_{-0.95}$, and $5.57^{+1.65}_{-1.65}10^{-6}$ arcmin², respectively. The overall S/N of our tSZ detection is 10.1σ , which is a vast improvement from the $2-3\sigma$ measurements we were able to obtain from previous data sets (Spacek et al. 2016, 2017).

Figure 5 shows the intensity spectrum of the dust and tSZ signals from our two-component fit for the two highest bins using the 2'.0 top-hat aperture. The dust spectrum is near the Rayleigh–Jeans limit, but it still contributes a significant signal at the lower frequencies when compared to the fainter tSZ. Some of the dust fit uncertainty arises from our inability to accurately determine the dust emissivity (β) and temperature ($T_{\rm dust}$), and would likely be helped by future experiments with more frequency channels.

The Compton-y measurements can further be converted into thermal energy following Equation (3), as was done in Section 5.2. Numerous steps were taken to verify the stacking process. Appendix A details the reproduction of previous studies (Planck Collaboration et al. 2013; Greco et al. 2015) to validate the stacking code used and compare catalog selection criteria. Fits made with different apertures and sizes are outlined in Appendix B.

5.2. Correction for Stellar Mass Uncertainty

At $0.5 \leqslant z \leqslant 1.5$ redshifts, our photometrically selected galaxies yield higher uncertainties in stellar mass than previous spectroscopic studies (Greco et al. 2015). To quantify our uncertainties in stellar mass, we performed two Monte Carlo tests. Using the final sample, we first perturbed the photometry using the 1σ photometric errors for each galaxy and band, and reran the SED-fitting code. This was repeated 100 times for each galaxy, and the standard deviation was computed for each galaxy. We found the mean uncertainty due to photometric errors to be $\sigma_{\log(M_p)} \simeq 0.140$ dex. Similarly, we repeated the procedure, this time keeping the photometry fixed, but perturbing the photometric redshift using a 5% uncertainty in 1+z, or $\sigma_z \approx 0.05(1+z)$. Again, this was repeated 100 times

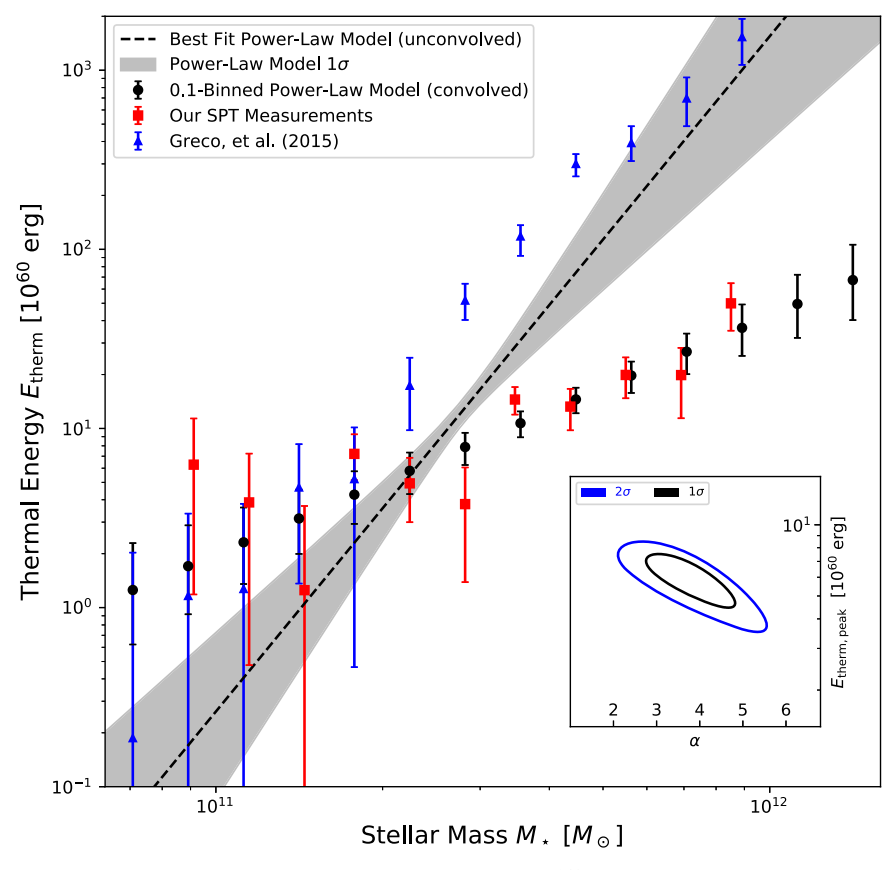


Figure 6. Energy-stellar mass plot of the best power-law fit (Equation (6), $E_{\text{therm,peak}} = 5.98^{+1.02}_{-1.00} \times 10^{60}$ erg, $\alpha = 3.77^{+0.60}_{-0.74}$) and shaded 1σ . Reconvolved thermal energy of 0.1-wide bins from the best fit with 1σ uncertainty (black circles), alongside our original SPT bin measurements (red squares) and those converted from Greco et al. (2015; blue triangles). Inset:Probability contour for the unconvolved power-law parameters $E_{\text{therm,peak}}$ and α , with lines at 1σ and 2σ .

for each galaxy, and we found the mean uncertainty due to photometric redshift errors to be $\sigma_{\log(M_2)} \simeq 0.074$ dex. These two numbers were combined in quadrature to give a total estimated uncertainty in stellar mass of $\sigma_{\log(M)} \simeq 0.16$ dex.

This 0.16 dex uncertainty is large enough to flatten our 0.1 dex stellar mass bin measurements by shifting a significant number of galaxies near the peak of the mass distribution into wings where they can overwhelm signal from the much smaller galaxy counts at low and high masses. As an illustration of this effect, Figure 9 in Appendix A shows the results of an additional 0.16 dex uncertainty applied to the low-redshift galaxies recreated from Greco et al. (2015).

Our high-redshift galaxies also contain this additional artifact from stellar mass uncertainty, but amplified further due to the narrower distribution of our sample. We correct for this by fitting our (\log_{10}) stellar mass distribution to a Gaussian, with a mass peak of $\log_{10}(M_{\star,\mathrm{peak}}/M_{\odot}) = 11.36 \pm 0.001$ and $\sigma = 0.20 \pm 0.001$. This allows for an easy deconvolution of the 0.16 dex stellar mass uncertainty, yielding an unconvolved distribution of $\sigma_{\mathrm{uncon.}} = \sqrt{(0.20)^2 - (0.16)^2} = 0.12$. We assign a simple power-law energy-mass function to the unconvolved distribution following

$$E_{\text{therm}} = E_{\text{therm,peak}} \left(\frac{M_{\star}}{M_{\star,\text{peak}}} \right)^{\alpha},$$
 (6)

where $M_{\star,\text{peak}} = 2.29 \times 10^{11} M_{\odot}$.

We assign the energies of this model to the unconvolved $(\sigma = 0.12) \log_{10}(M_{\star}/M_{\odot})$ distribution and convolve them with our 0.16 dex uncertainty. This brings our mass distribution

back to the original $\sigma=0.20$ Gaussian fit. The now-convolved assigned energies can then be placed in similar 0.1 dex stellar mass bins and fit to our measured SPT values to find $E_{\rm therm,peak}$ and α . Figure 6 shows the probability contour of our two-parameter fit (inset) and the corresponding unconvolved power-law relation with shaded 1σ , alongside the reconvolved 0.1-wide bin values used in the fit, our original SPT measurements, and thermal energies extracted from Greco et al. (2015).

This analysis reveals that thermal energy is indeed noticeably flattened at low- and high-mass bins for our stellar mass uncertainty of 0.16 dex. We extract a basic energy-stellar mass relation following Equation (6) with $E_{\rm therm,peak} = 5.98^{+1.02}_{-1.00} \times 10^{60}$ erg and $\alpha = 3.77^{+0.60}_{-0.74}$, indicative of the expected signal after stellar mass uncertainty correction. This relation also corresponds closely to the lower-redshift investigations of Planck Collaboration et al. (2013) and Greco et al. (2015).

5.3. Implications for AGN Feedback

While detailed constraints on AGN models are best carried out with comparisons to full numerical simulations, we can nevertheless draw general inferences from our constraints on $E_{\rm therm}$. The first of these is the remarkable similarity between our $z\approx 1$ results and those of Greco et al. (2015) at $z\approx 0.1$. It is important to note that these samples were selected by applying slightly different criteria. In our case, we apply cuts on age > 1 Gyr and SSFR < 0.01 Gyr⁻¹, while Greco et al. (2015) selected the locally brightest galaxies, defined as brighter than all other sample galaxies within a 1000 km/s redshift

difference and projected distance 1.0 Mpc. On the other hand, a wide range of theoretical models suggest a good match between the most massive quiescent galaxies at moderate redshifts and the central galaxies of massive halos in the nearby universe (e.g., Moster et al. 2013; Schaye et al. 2015; Pillepich et al. 2018).

This lack of significant evolution of thermal energy in the CGM around massive galaxies since $z \approx 1$ parallels the lack of significant evolution in the luminosity function of these galaxies (e.g., van Dokkum et al. 2010; Muzzin et al. 2013). All in all, this trend is slightly more compatible with models in which AGN feedback is dominated by radio-mode contributions. This is because in such models, gas accretion contributes to CGM heating, and radiative losses will contribute to CGM cooling. Whenever cooling exceeds heating, jets will arise that quickly push the gas up to the constant temperature and entropy at which cooling is inefficient. In quasar models, on the other hand, the energy input from feedback occurs once at high redshift, and gas is heated to the point that cooling is extremely inefficient up until today. In this case, gravitational heating will increase E_{therm} without any significant mechanism to oppose it. However, the particulars of this evolution are highly dependent on the history of galaxy and halo mergers between $0 < z \le 1$. Hence, it is possible that some types of quasar dominated models may be compatible with our measurements.

A second major inference is the overall level of feedback. As an estimate of the magnitude of gravitational heating, we can assume that the gas collapses and virializes along with an encompassing spherical dark matter halo, and is heated to the virial temperature $T_{\rm vir}$. This gives

$$E_{\text{therm,halo}}(M_{13}, z) = 1.5 \times 10^{60} \text{ erg } M_{13}^{5/3}(1+z),$$
 (7)

where M_{13} is the mass of the halo in units of $10^{13} M_{\odot}$ (Spacek et al. 2016). For massive elliptical galaxies, we can convert from halo mass into galaxy stellar mass using the observed relation between black hole mass and halo circular velocity (Ferrarese 2002) and the relation between black hole mass and bulge dynamical (Marconi & Hunt 2003). As shown in Spacek et al. (2016), this gives

$$E_{\text{therm,gravity}}(M_{\star}, z) \approx 5 \times 10^{60} \,\text{erg} \, \frac{M_{\star}}{10^{11} M_{\odot}} (1 + z)^{-3/2}.$$
 (8)

This is the total thermal energy expected around a galaxy of stellar mass M_{\star} ignoring both radiative cooling and feedback. For a mean redshift of ≈ 1.1 and $M_{\star,\mathrm{peak}} = 2.29 \times 10^{11} M_{\odot}$, this gives $\approx 4 \times 10^{60}$ erg. This estimate has an uncertainty of about a factor of two, which is significantly larger than the uncertainty in our measurements. Nevertheless, it is somewhat lower than $E_{\mathrm{therm,peak}} = 5.98^{+1.02}_{-1.00} \times 10^{60}$ erg, suggesting the presence of additional nongravitational heating, particularly as cooling losses are not included in Equation (8).

As a simple estimate of heating due to quasar-mode feedback, we can make use of the model described in Scannapieco & Oh (2004), which gives

$$E_{\rm therm,feedback}(M_{\star}, z) \approx 4 \times 10^{60} \, {\rm erg} \, \epsilon_{k,0.05} \frac{M_{\star}}{10^{11} M_{\odot}} \, (1 + z)^{-3/2}$$
 (9)

where $\epsilon_{k,0.05}$ is the fraction of the bolometric luminosity of the quasar associated with an outburst, normalized by a fiducial

value of 5%, which is typical of quasar models (e.g., Scannapieco & Oh 2004; Thacker et al. 2006; Costa et al. 2014). For the peak mass and average redshift of our sample, this gives $\approx \epsilon_{k,0.05} 3 \times 10^{60}$ erg. Taking $\epsilon_{k,0.05} = 1$ and adding this to contribution from $E_{\text{therm,gravity}}$ above gives a total energy of $\approx 7 \times 10^{60}$ erg. This is on the high side of our measurements, but as it does not account for any energy losses, it appears to be a somewhat better match than models without nongravitational heating.

Finally, radio-mode models are expected to fall somewhere between these two limits, with jets supplying power to roughly balance cooling processes, but never adding a large burst of additional energy of the type estimated in Equation (9). This would suggest a somewhat better match to the data than pure-gravitational heating models, but again with far too much theoretical uncertainty to draw any definite conclusions.

A third major inference from our measurements comes from the slope of Equation (6), which is significantly steeper than in our simple models. This is most likely due to uncertainties in the halo-mass stellar mass relation, which are particularly large for the most massive $z \approx 1$ galaxies (Wang et al. 2013; Lu et al. 2015; Moster et al. 2018; Kravtsov et al. 2018; Behroozi et al. 2010, 2019). This represents a major change in the field from only a few years ago, in which tSZ detections at halo masses lower than galaxy clusters were only marginal and provided only weak constraints on feedback. Rather, our measurements, along with other recent constraints (Schaan et al. 2021; Amodeo et al. 2021), make it clear that observations are fast outstripping theoretical estimates, and that future close comparisons between measurements and full simulations will yield significant new insights into the history of AGN feedback.

5.4. Two-halo Effect

It is important to recognize that our measurements include the contribution not only from the selected galaxies, but also from the excess of galaxies clustered around them. This so-called two-halo contribution is described in detail in Hill et al. (2018), who showed this to be significant for lower-redshift galaxies and clusters. To estimate the impact of this effect on our $z \approx 1$ sample, we can again make use of a simple model for gravitational heating as given by Equation (7). This allows us to compute the excess energy due to the neighboring halos within a radius R perpendicular to a central galaxy of halo mass M_0 as

$$E_{\text{therm,2halo}} = b(M_0) \int_{10^{11} \,\mathrm{M_\odot}}^{10^{16} \,\mathrm{M_\odot}} \frac{dn(M,z)}{dM} E_{\text{therm,halo}}(M,z) b(M) dM$$

$$\times \int_{-100R}^{100R} 2\pi \int_0^R dr \ r \ \xi(\sqrt{r^2 + l^2}, z) dr \ dl,$$
(10)

where we account for the excess of neighboring halos with masses between $10^{11}-10^{16}~M_{\odot}$ within a cylinder of radius R and length 200R. In this expression, dn(M,z)/dM is the number density of dark matter halos per unit mass, $\xi(r,z)$ is the dark matter correlation function, and $b(M)=1+(\nu^2-1)/1.69$ (with $\nu\equiv 1.69\sigma(M,z)^{-1}$) is the bias factor that accounts for mass-dependent differences between the underlying dark matter density field and the distribution of massive dark matter halos (Mo & White 1996).

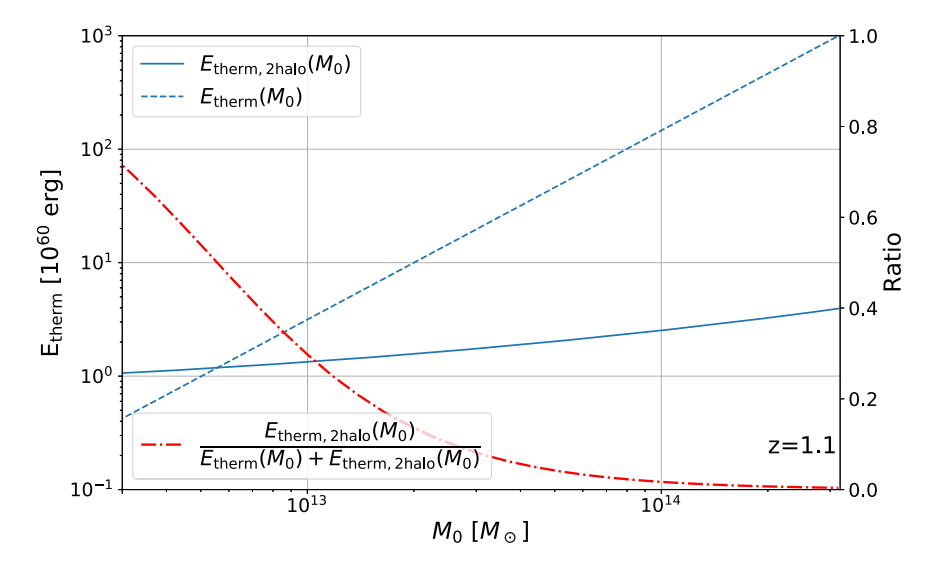


Figure 7. Contribution to the thermal energy from a two-halo term. The dashed blue line is an estimate of the gravitational thermal energy in the CGM of a galaxy with a given halo mass (x-axis). The solid blue line estimates the total thermal energy in a cylinder (radius = 2 Mpc × len = 400 Mpc) centered and stacked on a galaxy with a given halo mass. This estimate uses the two-point correlation function to include galaxies within the cylinder given the mass of the central galaxy, M_0 (see details in the text). All data are for z = 1.1. The dot-dashed red line indicates the ratio of the energy in the cylinder to the sum of both curves and uses the y-axis to the right, which shows that the central halo dominates the total energy when its mass exceeds $\approx 10^{13} M_{\odot}$ or when E_{therm} exceeds $\approx 3 \times 10^{60}$ erg.

In Figure 7 we compare the energy in the central halo given by Equation (7) to the two-halo contribution given by Equation (10) over the range of halo masses from $M_0 = 10^{12.5} - 10^{14.5} M_{\odot}$. In this figure, we use the code for anisotropies in the microwave background (Lewis & Challinor 2011) to compute the dark matter correlation function, $\xi(r,z)$, and the rms fluctuations at a redshift z within a sphere containing a mass M, $\sigma(M,z)$, and we compute the number density of halos, dn(M,z)/dM, according to the standard Press & Schechter (1974) formula.

While the relation between galaxy stellar mass and halo mass at $z \approx 1.1$ is uncertain, as mentioned above, the fact that the central halo becomes $E_{\rm therm} \gg E_{\rm therm,2halo}$ when the total thermal energy exceeds $\approx 3 \times 10^{60}$ erg suggests that the majority of our measurements are in the range for which the central halo is dominant. The reason that the two-halo term is significantly less important than at $z \approx 0$ is that the dark matter structures have had less time to collapse, meaning that the matter correlation function ξ is significantly smaller at $z \approx 1$ than it is today. Thus, although this effect merits careful consideration in comparisons with simulations, it is less likely to complicate the analysis to the degree it does for more local samples (e.g., Schaan et al. 2021). In addition, although this cannot be computed directly from Equation (10), the two-halo contribution is likely to become more important on sightlines with large impact parameters from the selected galaxies, and thus it is important to keep in mind when interpreting the tSZ radial profile, a topic to which we turn our attention in the next section.

5.5. Radial Profile

The radial profile of the tSZ signal has recently been studied at lower redshifts with the latest ACT release at similar angular resolution (Schaan et al. 2021). To compare against this study, we apply the same procedure as in Schaan et al. (2021) to compute this profile: summing within a cap or top-hat shape of radius R, and subtracting the neighboring pixels out to $\sqrt{2}R$ to remove the surrounding background offset such as from the

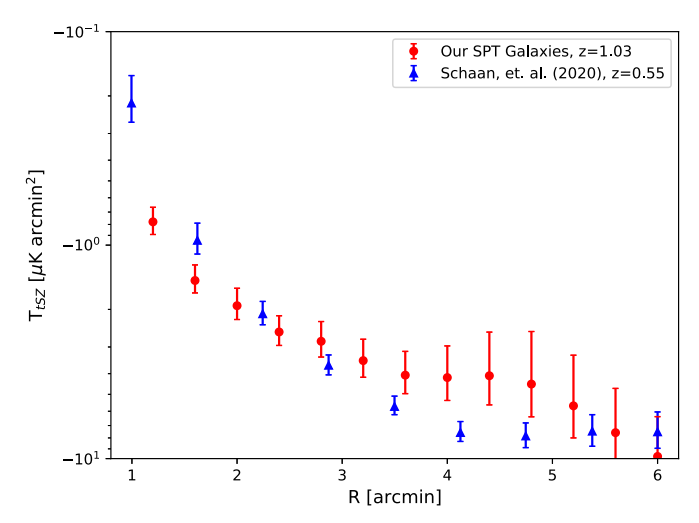


Figure 8. Radial profile of our complete (N=138235) SPT galaxy catalog (red circles, 1 arcmin = 1.01 comoving Mpc = 0.50 proper Mpc @z=1.03), alongside the recent profile from Schaan et al. (2021; blue triangles, 1 arcmin = 0.61 comoving Mpc = 0.39 proper Mpc @z=0.55). The y-axis is in units of integrated CMB temperature at 150 GHz (μ K arcmin²). The two profiles are similar even with their difference in redshift.

primary CMB. In this case, we abstain from the high-pass filtering done in our main stellar mass bin analysis.

The profile of our SPT galaxies is shown in Figure 8, where it is compared to the CMASS sample in Schaan et al. (2021), which has a mean redshift of z=0.55, and the mean $\log_{10}(M_\star/M_\odot)$ in linear units is $\approx 2\times 10^{11}M_\odot$. As a preliminary analysis, we stack all N = 138,325 SPT galaxies, and apply the same style aperture from R=1.2-6.2 arcmin radius at each band. We then use our two-component fit of Equation (4) using the median redshift of z=1.03, and dust parameters $T=20\pm 5\mathrm{K}$ and $\beta=1.75\pm 0.25$ applied as before. The final tSZ values are converted into integrated CMB temperature with respect to 150 GHz, as in Schaan et al. (2021). The two tSZ profiles have very similar overall shapes. Our profile, however,

is slightly less clearly defined with larger uncertainty because it is at higher redshift and uses a smaller sample size. A more detailed comparison, such as by mass-binning and fitting to profile models, is left for future work.

6. Discussion

From $z \approx 1$ to $z \approx 0$, dark matter halos continue to merge and accrete material, but the growth of massive galaxies over this redshift range is minimal, with $\log_{10}(M_\star/M_\odot) = 11.15$ galaxies growing in mass by less than 0.2 dex (Muzzin et al. 2013). To explain this surprising trend, theoretical models have been forced to invoke significant energy input from AGN that heats the medium surrounding massive galaxies to temperatures high enough to prevent it from cooling and forming further generations of stars. On the other hand, such AGN feedback is largely unconstrained by observations.

Here we make use of measurements of the tSZ effect to derive direct constraints that can be applied to such models. As the total tSZ distortion along a given sightline is proportional to the line-of-sight integral of the pressure, the total signal summed over the area of sky around any object is proportional to the volume integral of the pressure, or the total thermal energy. This means that by summing the Compton distortions over the patches of sky around galaxies, we can directly measure the thermal energy of the CGM surrounding them.

We apply this technique to constrain the signal of 138,235 $z \approx 1$ galaxies, selected from the DES and WISE surveys. Data from the SPT at 95, 150, and 220 GHz were stacked around the galaxies, spatially filtered to separate the signal from primary CMB fluctuations, and fit with a graybody model to remove the dust contribution, which is detected with an S/N of 9.8σ . The resulting tSZ around these galaxies is detected with an overall S/N of 10.1σ , which is high enough to allow us to partition the galaxies into 0.1 dex stellar mass bins from $M_{\star} = 10^{10.9} M_{\odot} - 10^{12} M_{\odot}$, which have corresponding tSZ detections of up to 5.6σ . We also observe significantly more dust at these frequencies than previous low-redshift studies (Planck Collaboration et al. 2013; Greco et al. 2015), and a noticeable increase in dust signal with higher-mass bins.

As the stellar mass distribution of our selected galaxies is highly peaked at $M_{\star,\mathrm{peak}} = 2.3 \times 10^{11} M_{\odot}$, the 0.16 dex uncertainty in our photometric fits to the masses is large enough to flatten our measurements, shifting a significant number of galaxies near the distribution peak into wings where they can overwhelm signal from the much smaller galaxy counts at low and high masses. To correct for this effect, we carry out a two-parameter fit for the unconvolved energy-mass relation that best fits our data, of the form $E_{\text{therm}} = E_{\text{therm,peak}} (M_{\star}/M_{\star,\text{peak}})^{\alpha}$. In this case, we find an amplitude at the mass peak of $E_{\text{therm,peak}} = 5.98^{+1.02}_{-1.00} \times 10^{60}$ erg and a slope of $\alpha = 3.77^{+0.60}_{-0.74}$. This, however, would not take into account any inherent biases in our stellar mass uncertainty, such as a potentially smaller uncertainty for our brighter, more massive galaxies.

This aligns well with previous $z \approx 0$ studies, indicating a good match between the thermal energy of the CGM surrounding the most massive quiescent galaxies at moderate redshifts and the central galaxies of massive halos in the nearby universe. When compared to theoretical models, our energy-mass relation best corresponds to moderate radio-mode feedback. Purely gravitational heating predictions are slightly lower than the final results, while quasar-mode AGN feedback

models are slightly higher. However, all of these models have wide enough uncertainties that definitive conclusions are difficult to be drawn from them. This means that observations are no longer in the regime of marginal detections, and are quickly outstripping the capabilities of theoretical estimates. This further highlights the need for improved theoretical models to keep pace with the ever-increasing observational capabilities.

The limitations in our observational analysis primarily stem from our ability to accurately fit and remove the large dust component such as seen in the galaxy stacks in Figure 4 and the dust fit in Figure 5. The dust-fit amplitude is set mainly by the 220 GHz band, and we use a spectral emissivity index β and dust temperature $T_{\rm dust}$ with large uncertainty due to our inability to fit them with only three frequency bands. The addition of a similar resolution survey at far-infrared frequencies would provide a better fit of all thermal dust parameters.

We also recognize there is a likely two-halo contribution term for these stacking type measurements, which was shown to be large in Hill et al. (2018) for lower-redshift galaxies and clusters. While simple models such as presented in Section 5.4 suggest that the contribution of this effect to the total SZ signal is small for the majority of our $z \approx 1$ galaxies, the exact significance of the two-halo contribution to our measurements of the radial profile is yet to be determined.

An initial radial tSZ profile of our entire galaxy sample in Section 5.5 highlights the similarities with lower-redshift studies (Schaan et al. 2021). Additional investigation is needed to refine and compare to profile models, including the impact of additional sources such as the aforementioned two-halo term.

Surveys with similar resolution across more of the sky, such as planned with the next generation Atacama Cosmology Telescope instrument (Advanced ACTPol Koopman et al. 2018), will enable a larger sampling area. Likewise, advances in spatial resolution, such as will be possible using the TolTEC camera being built for the 50 m Large Millimeter-wave Telescope (Bryan et al. 2018), will allow for a cleaner separation between the tSZ signal, which comes primarily from the CGM, and the dust signal, which comes primarily from the underlying galaxy. These developments promise to yield dramatic new insights into the physical processes that shaped the most massive galaxies in the universe.

We thank Alexander Van Engelen for helpful discussions and the referee for detailed comments that greatly improved this work. We acknowledge Research Computing at Arizona State University for providing HPC resources that have contributed to the research results reported within this paper. The galaxy data used here was from DES and WISE, while the maps are publicly obtained from SPT. This publication makes use of data products from the Wide-field Infrared Survey Explorer, which is a joint project of the University of California, Los Angeles, and the Jet Propulsion Laboratory/ California Institute of Technology, and NEOWISE, which is a project of the Jet Propulsion Laboratory/California Institute of Technology. WISE and NEOWISE are funded by the National Aeronautics and Space Administration. The manipulation of the maps was aided by the *Healpy* python module for Healpix operations. E.S. was supported by NSF grant AST-1715876.

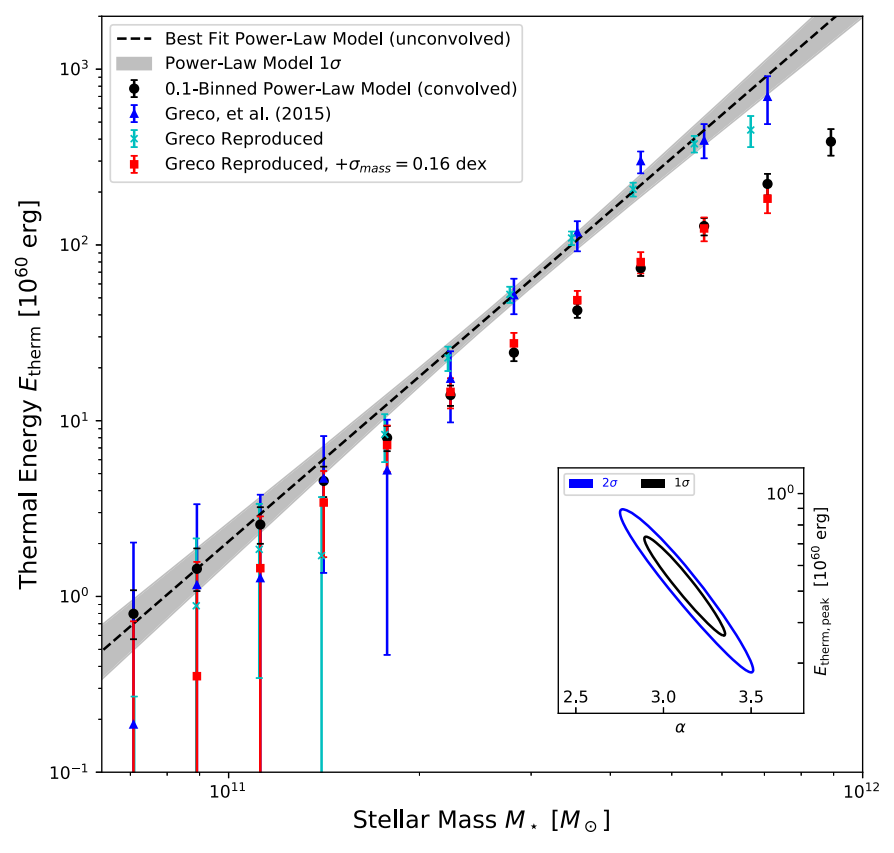


Figure 9. Low-z galaxies observed in Greco et al. (2015) converted into thermal energy (blue triangles). We also recreated the low-z galaxy sample as described in Greco et al. (2015) and Planck Collaboration et al. (2013) and obtained similar results (cyan crosses). Finally, a major concern with our high-z SPT galaxies is the larger uncertainty in mass ($\sigma_m = 0.16$ dex). When we use the recreated low-z galaxies, an additional $\sigma_m = 0.16$ dex uncertainty in mass shows diluted signal in the higher stellar mass bins, indicating that our high-z galaxies contain this effect (red squares). Error bars represent 1σ uncertainties. We also then show our energy-mass function of Equation (6) applied to the flattened bins, producing a slope that aligns well with the original values. The flattened power-law bins used in the fit are shown as well (black circles).

Appendix A Reproduction of Previous Low Redshift Results

To ensure there were no unknown errors in the stacking procedure and code, we reconstructed the locally brightest galaxy catalog used in the studies of Planck Collaboration et al. (2013) and Greco et al. (2015) and stacked them with the Planck Modified Internal Linear Combination Algorithm (MILCA) Compton-y map.

The catalog was selected in identical fashion as in Planck Collaboration et al. (2013) and Greco et al. (2015). Starting from the spectroscopic New York University Value Added Galaxy Catalog⁶ (Blanton et al. 2005), which uses the Sloan Digital Sky Survey (SDSS) DR7, r < 17.7 magnitude and z > 0.03 cuts were first applied. Then any smaller neighbors of the catalog were removed by selecting only galaxies brighter than all other sample galaxies within a 1000 km/s redshift difference and a projected distance of 1.0 Mpc. This method was then repeated with a separate photometric catalog, photoz2 (Cunha et al. 2009). After a final removal of any galaxies within Planck point sources and 40% galactic masks, 243364 galaxies were obtained. This is a marginally smaller number than that reported in Planck Collaboration et al. (2013), likely from a slightly stricter removal of flagged galaxies or updated masks. Since spectroscopic and low redshift, these have a lower

stellar mass uncertainty of \approx 0.1 dex (Blanton & Roweis 2007) than our photometric and high-z catalog (\approx 0.16 dex). We bin the low-z galaxies in similar $\log_{10}(M_{\star}/M_{\odot})$ 0.1-wide mass bins.

The map used for stacking is a component-separated MILCA from Planck DR2⁷ (Planck Collaboration et al. 2016d). This map has units of microCompton-y and a FWHM of 10 arcmin. For simplicity, we use an R = 10 arcmin radius top-hat aperture and mean-subtract with an annulus from R to R+FWHM. The average equal-weighted signals from mass bins of $10.0 < \log_{10}(M_{\star}/M_{\odot}) < 11.9$ are shown in Figure 9, converted into thermal energy as in Equation (3). Even without simulations for inverse-variance weighting and variable aperture radii, our results compare well with those of Greco et al. (2015), which are also plotted in Figure 9.

To determine the effect of our larger ≈ 0.16 dex mass uncertainty in our original high-z catalog, we apply a 0.16 dex Gaussian uncertainty to all low-z galaxy masses. By providing a new weighted mass-binning according to the likelihood of each galaxy to be in each respective bin, we calculate the new average thermal energies with the 0.16 dex mass uncertainty (also shown in Figure 9). These values reveal a dimming of the signal at high masses, due to contamination from low-mass galaxies shifted higher from the uncertainty. This is likely to be similar for our high-z galaxies and provides a challenge to

⁶ https://sdss.physics.nyu.edu/vagc/

⁷ https://irsa.ipac.caltech.edu/data/Planck/release_2/all-sky-maps/ysz_index.html

Table 3
Results for Alternate Aperture Shapes and Sizes: the Fiducial 2'.0 Radius Top-hat, a Larger 4'.0 Radius Top-hat, a 3'.0 FWHM Gaussian, and a 6'.0 FWHM Gaussian

	$\log_{10}(M_{\star}/M_{\odot})$	2:0	4:0	3:0	6:0
	-10 , -	Top-Hat	Top-Hat	Gaussian	Gaussian
$\int y(\vec{\theta})d\vec{\theta} \ [10^{-6} \ \text{arcmin}^2]$					
	10.9 - 11.0	$0.78^{+0.63}_{-0.63}$	$1.23^{+1.35}_{-1.35}$	$0.72^{+0.61}_{-0.61}$	$0.90^{+1.02}_{-1.02}$
	11.0 - 11.1	$0.47^{+0.41}_{-0.42}$	$0.79^{+0.87}_{-0.87}$	$0.55^{+0.40}_{-0.40}$	$0.61^{+0.66}_{-0.66}$
	11.1 - 11.2	$0.15^{+0.30}_{-0.30}$	$0.15^{+0.63}_{-0.63}$	$0.14^{+0.29}_{-0.29}$	$0.31^{+0.48}_{-0.48}$
	11.2 - 11.3	$0.87^{+0.25}_{-0.25}$	$0.79^{+0.52}_{-0.52}$	$0.81^{+0.24}_{-0.24}$	$0.91^{+0.39}_{-0.39}$
	11.3 - 11.4	$0.59^{+0.23}_{-0.23}$	$1.10^{+0.48}_{-0.48}$	$0.59^{+0.22}_{-0.22}$	$0.91^{+0.36}_{-0.36}$
	11.4 - 11.5	$0.44^{+0.27}_{-0.28}$	$0.00^{+0.52}_{-0.53}$	$0.39^{+0.25}_{-0.27}$	$0.06^{+0.39}_{-0.41}$
	11.5 - 11.6	$1.69^{+0.29}_{-0.30}$	$2.42^{+0.60}_{-0.61}$	$1.63^{+0.28}_{-0.29}$	$2.12^{+0.46}_{-0.46}$
	11.6 - 11.7	$1.52^{+0.39}_{-0.40}$	$1.76^{+0.81}_{-0.82}$	$1.38^{+0.38}_{-0.39}$	$1.65^{+0.62}_{-0.62}$
	11.7 - 11.8	$2.27^{+0.57}_{-0.59}$	$2.90^{+1.18}_{-1.19}$	$2.20^{+0.56}_{-0.57}$	$2.42^{+0.90}_{-0.91}$
	11.8 - 11.9	$2.23^{+0.94}_{-0.95}$	$0.32^{+1.99}_{-2.02}$	$2.06^{+0.91}_{-0.92}$	$1.12^{+1.50}_{-1.53}$
	11.9 - 12.0	$5.57^{+1.65}_{-1.65}$	$3.78^{+3.47}_{-3.47}$	$4.91^{+1.59}_{-1.60}$	$3.45^{+2.63}_{-2.63}$
$E_{\text{therm,peak}}$ [10 ⁶	o erg]	$5.98^{+1.02}_{-1.00}$	$7.62_{-2.06}^{+1.83}$	$5.76^{+0.99}_{-0.96}$	$7.17^{+1.44}_{-1.55}$
α		$3.77^{+0.60}_{-0.74}$	$2.93^{+0.94}_{-1.33}$	$3.65^{+0.60}_{-0.76}$	$2.88^{+0.82}_{-1.08}$

Note. Listed are the respective Compton-y parameter fits found from Equation (4), and the final two rows show the stellar mass uncertainty correction power-law fit parameters $E_{therm,peak}$ and α . As expected, the additional noise from the larger apertures results in worse fits. The 3...0 Gaussian aperture behaves similar to that of our 2...0 arcmin top-hat chosen for the main results.

accurately correct for. Our method that aimed at correcting for this (in Section 5.2 and Equation (6)) can similarly be applied to these purposely dimmed values to obtain $E_{\rm therm,peak}=0.53^{+0.14}_{-0.11}$ erg and $\alpha=3.12^{+0.12}_{-0.19}$ about a peak mass of $\log_{10}(M_{\star,peak}/M_{\odot})=11.8$. As shown in Figure 9, this aligns well with the expected original results, and the slope α is near the $3.77^{+0.60}_{-0.74}$ extracted from our SPT sample in Section 5.2.

Later studies (Hill et al. 2018) have also shown that a residual two-halo effect occurs for this low-redshift catalog, which is more evident at the low masses. In some instances, the two-halo contribution was shown to dominate, but further investigation is needed to translate this into our higher-redshift galaxies.

Appendix B Impact of Aperture Size

The aperture shape and size used in the integrated sums at each frequency have a large influence on the final two-component fit of Equation (4). It needs to be large enough to encompass most of the signal from our galaxies without being too large to introduce extra noise and nearby source contamination.

Table 3 shows the $\log_{10}(M_{\star}/M_{\odot})$ 0.1 wide bin Compton-y fits alongside the final stellar mass correction power-law parameters $E_{\rm therm,peak}$ and α for three other potential aperture choices. A 3.0 FWHM Gaussian aperture is chosen as a similar comparison to our main 2.0 top-hat used. Two larger apertures, a 4.0 top-hat and a 6.0 Gaussian, are also selected to highlight the additional noise they incur.

ORCID iDs

Jeremy Meinke https://orcid.org/0000-0003-0636-2101 Seth Cohen https://orcid.org/0000-0003-3329-1337 Evan Scannapieco https://orcid.org/0000-0002-3193-1196 Richard Sarmento https://orcid.org/0000-0002-8013-5970

References

```
Abbott, T. M. C., Abdalla, F. B., Allam, S., et al. 2018, ApJS, 239, 18
Addison, G. E., Dunkley, J., & Bond, J. R. 2013, MNRAS, 436, 1896
Amodeo, S., Battaglia, N., Schaan, E., et al. 2021, PhRvD, 103, 063514
Battaglia, N., Bond, J. R., Pfrommer, C., Sievers, J. L., & Sijacki, D. 2010,
   ApJ, 725, 91
Behroozi, P., Wechsler, R. H., Hearin, A. P., & Conroy, C. 2019, MNRAS,
  488, 3143
Behroozi, P. S., Conroy, C., & Wechsler, R. H. 2010, ApJ, 717, 379
Blanton, M. R., & Roweis, S. 2007, AJ, 133, 734
Blanton, M. R., Schlegel, D. J., Strauss, M. A., et al. 2005, AJ, 129, 2562
Bleem, L. E., Stalder, B., de Haan, T., et al. 2015, ApJS, 216, 27
Bocquet, S., Dietrich, J. P., Schrabback, T., et al. 2019, ApJ, 878, 55
Bower, R. G., Benson, A. J., Malbon, R., et al. 2006, MNRAS, 370, 645
Brammer, G. B., van Dokkum, P. G., & Coppi, P. 2008, ApJ, 686, 1503
Bruzual, G., & Charlot, S. 2003, MNRAS, 344, 1000
Bryan, S., Austermann, J., Ferrusca, D., et al. 2018, Proc. SPIE, 10708,
   107080J
Chamberlain, C., Arav, N., & Benn, C. 2015, MNRAS, 450, 1085
Chartas, G., Brandt, W. N., Gallagher, S. C., & Proga, D. 2007, AJ, 133,
Chatterjee, S., Ho, S., Newman, J. A., & Kosowsky, A. 2010, ApJ, 720, 299
Chown, R., Omori, Y., Aylor, K., et al. 2018, ApJS, 239, 10
Churazov, E., Brüggen, M., Kaiser, C. R., Böhringer, H., & Forman, W. 2001,
    pJ, 554, 261
Coleman, G. D., Wu, C. C., & Weedman, D. W. 1980, ApJS, 43, 393
Costa, T., Sijacki, D., & Haehnelt, M. G. 2014, MNRAS, 444, 2355
Cowie, L. L., Songaila, A., Hu, E. M., & Cohen, J. G. 1996, AJ, 112, 839
Crichton, D., Gralla, M. B., Hall, K., et al. 2016, MNRAS, 458, 1478
Croton, D. J., Springel, V., White, S. D. M., et al. 2006, MNRAS, 365, 11
Cunha, C. E., Lima, M., Oyaizu, H., Frieman, J., & Lin, H. 2009, MNRAS,
de Kool, M., Arav, N., Becker, R. H., et al. 2001, ApJ, 548, 609
Draine, B. T. 2011, Physics of the Interstellar and Intergalactic Medium
  (Princeton, NJ: Princeton Univ. Press)
Drory, N., & Alvarez, M. 2008, ApJ, 680, 41
Dunn, J. P., Bautista, M., Arav, N., et al. 2010, ApJ, 709, 611
Fabian, A. C. 2012, ARA&A, 50, 455
Ferrarese, L. 2002, ApJ, 578, 90
Feruglio, C., Maiolino, R., Piconcelli, E., et al. 2010, A&A, 518, L155
Gralla, M. B., Crichton, D., Marriage, T. A., et al. 2014, MNRAS, 445, 460
Granato, G. L., De Zotti, G., Silva, L., Bressan, A., & Danese, L. 2004, ApJ,
Greco, J. P., Hill, J. C., Spergel, D. N., & Battaglia, N. 2015, ApJ, 808, 151
```

```
Greene, J. E., Pooley, D., Zakamska, N. L., Comerford, J. M., & Sun, A.-L.
   2014, ApJ, 788, 54
Hall, K. R., Zakamska, N. L., Addison, G. E., et al. 2019, MNRAS, 490, 2315
Hand, N., Appel, J. W., Battaglia, N., et al. 2011, ApJ, 736, 39
Harrison, C. M., Alexander, D. M., Mullaney, J. R., & Swinbank, A. M. 2014,
    MNRAS, 441, 3306
Hill, J. C., Baxter, E. J., Lidz, A., Greco, J. P., & Jain, B. 2018, PhRvD, 97,
Hilton, M., Hasselfield, M., Sifón, C., et al. 2018, ApJS, 235, 20
Hojjati, A., Tröster, T., Harnois-Déraps, J., et al. 2017, MNRAS, 471, 1565
Ishihara, D., Onaka, T., Kataza, H., et al. 2010, A&A, 514, A1
Joint Iras Science, W. G. 1994, vCat, II/125
Kinney, A. L., Calzetti, D., Bohlin, R. C., et al. 1996, ApJ, 467, 38
Koopman, B. J., Cothard, N. F., Choi, S. K., et al. 2018, JLTP, 193, 1103
Kravtsov, A. V., Vikhlinin, A. A., & Meshcheryakov, A. V. 2018, AstL, 44, 8
Lacy, M., Mason, B., Sarazin, C., et al. 2019, MNRAS, 483, L22
Lansbury, G. B., Jarvis, M. E., Harrison, C. M., et al. 2018, ApJL, 856, L1
Lewis, A., & Challinor, A. 2011, CAMB: Code for Anisotropies in the
  Microwave Background, ascl:1102.026
Lu, Z., Mo, H. J., Lu, Y., et al. 2015, MNRAS, 450, 1604
Mainzer, A., Bauer, J., Grav, T., et al. 2011, ApJ, 731, 53
Marconi, A., & Hunt, L. K. 2003, ApJL, 589, L21
McNamara, B. R., Russell, H. R., Nulsen, P. E. J., et al. 2016, ApJ, 830, 79
McNamara, B. R., Wise, M., Nulsen, P. E. J., et al. 2000, ApJL, 534, L135
Miller, T. R., Arav, N., Xu, X., & Kriss, G. A. 2020, MNRAS, 499, 1522
Mo, H. J., & White, S. D. M. 1996, MNRAS, 282, 347
Moster, B. P., Naab, T., & White, S. D. M. 2013, MNRAS, 428, 3121
Moster, B. P., Naab, T., & White, S. D. M. 2018, MNRAS, 477, 1822
Mroczkowski, T., Nagai, D., Basu, K., et al. 2019, SSRv, 215, 17
Muzzin, A., Marchesini, D., Stefanon, M., et al. 2013, ApJ, 777, 18
Oke, J. B., & Gunn, J. E. 1983, ApJ, 266, 713
Piffaretti, R., Arnaud, M., Pratt, G. W., Pointecouteau, E., & Melin, J. B. 2011,
     &A, 534, A109
Pillepich, A., Nelson, D., Hernquist, L., et al. 2018, MNRAS, 475, 648
Planck Collaboration, Ade, P. A. R., Aghanim, N., et al. 2011, A&A, 536, A8
Planck Collaboration, Ade, P. A. R., Aghanim, N., et al. 2013, A&A, 557, A52
Planck Collaboration, Ade, P. A. R., Aghanim, N., et al. 2014, A&A, 571, A28
Planck Collaboration, Ade, P. A. R., Aghanim, N., et al. 2014, A&A, 564, A45
Planck Collaboration, Ade, P. A. R., Aghanim, N., et al. 2016a, A&A, 594, A24
```

```
Planck Collaboration, Ade, P. A. R., Aghanim, N., et al. 2016b, A&A,
  594, A27
Planck Collaboration, Ade, P. A. R., Aghanim, N., et al. 2016c, A&A,
  594, A28
Planck Collaboration, Aghanim, N., Arnaud, M., et al. 2016d, A&A, 594, A22
Planck Collaboration, Aghanim, N., Akrami, Y., et al. 2020, A&A, 641, A6
Press, W. H., & Schechter, P. 1974, ApJ, 187, 425
Rees, M. J., & Ostriker, J. P. 1977, MNRAS, 179, 541
Reichardt, C. L., Stalder, B., Bleem, L. E., et al. 2013, ApJ, 763, 127
Ruan, J. J., McQuinn, M., & Anderson, S. F. 2015, ApJ, 802, 135
Santini, P., Ferguson, H. C., Fontana, A., et al. 2015, ApJ, 801, 97
Scannapieco, E., & Oh, S. P. 2004, ApJ, 608, 62
Scannapieco, E., Thacker, R. J., & Couchman, H. M. P. 2008, ApJ, 678, 674
Schaan, E., Ferraro, S., Amodeo, S., et al. 2021, PhysRevD, 103, 063513
Schaffer, K. K., Crawford, T. M., Aird, K. A., et al. 2011, ApJ, 743, 90
Schaye, J., Crain, R. A., Bower, R. G., et al. 2015, MNRAS, 446, 521
Schlafly, E. F., Meisner, A. M., & Green, G. M. 2019, ApJS, 240, 30
Silk, J., & Rees, M. J. 1998, A&A, 331, L1
Spacek, A., Scannapieco, E., Cohen, S., Joshi, B., & Mauskopf, P. 2016, ApJ,
  819, 128
Spacek, A., Scannapieco, E., Cohen, S., Joshi, B., & Mauskopf, P. 2017, ApJ,
  834, 102
Springel, V., Pakmor, R., Pillepich, A., et al. 2018, MNRAS, 475, 676
Sunyaev, R. A., & Zeldovich, Y. B. 1972, CoASP, 4, 173
Sunyaev, R. A., & Zeldovich, Y. B. 1980, MNRAS, 190, 413
Thacker, R. J., Scannapieco, E., & Couchman, H. M. P. 2006, ApJ, 653, 86
Treu, T., Ellis, R. S., Liao, T. X., & van Dokkum, P. G. 2005, ApJL, 622, L5
van Dokkum, P. G., Whitaker, K. E., Brammer, G., et al. 2010, ApJ, 709,
Veilleux, S., Meléndez, M., Sturm, E., et al. 2013, ApJ, 776, 27
Voges, W., Aschenbach, B., Boller, T., et al. 1999, A&A, 349, 389
Wampler, E. J., Chugai, N. N., & Petitjean, P. 1995, ApJ, 443, 586
Wang, L., Farrah, D., Oliver, S. J., et al. 2013, MNRAS, 431, 648
Werner, N., McNamara, B. R., Churazov, E., & Scannapieco, E. 2019, SSRv,
  215. 5
White, S. D. M., & Frenk, C. S. 1991, ApJ, 379, 52
Wright, E. L., Eisenhardt, P. R. M., Mainzer, A. K., et al. 2010, AJ, 140,
Yamamura, I., Makiuti, S., Ikeda, N., et al. 2010, yCat, II/298
```